Optimal design of helical heat/mass exchangers under laminar flow: CFD investigation and correlations for maximal transfer efficiency and process intensification performances

Omran Abushammala, Rainier Hreiz, Cécile Lemaitre, Eric Favre

Optimal design of helical heat/mass exchangers under laminar flow: CFD investigation and correlations for maximal transfer efficiency and process intensification performances

Omran Abushammala, Rainier Hreiz*, Cécile Lemaître, Éric Favre

Laboratoire Réactions et Génie des Procédés, Université de Lorraine, CNRS, LRGP, F-54000 Nancy, France.
*Corresponding author at:
Rainier Hreiz, Laboratoire Réactions et Génie des Procédés, Université de Lorraine, ENSIC, CNRS, LRGP, 1 rue Grandville, 54001 Nancy, France. Tel: +33 (0) 372 743 876; E-mail address: rainier.hreiz@univ-lorraine.fr

Abstract

Highly curved helical pipes (HCHPs) offer tremendous potentialities for intensified heat/mass transfer performances as they generate intense Dean-type vortices. However, these designs have not been explored so far in the literature, probably because they are difficult to build using traditional manufacturing techniques. Nowadays, thanks to a witnessed progress in 3D-printing, the fabrication of HCHPs has become achievable. Therefore, investigating their performance in terms of heat and mass transfer intensification presents significant interest from both academic and industrial points of view.

In this paper, CFD simulations are carried out to determine the heat/mass transfer efficiency in helical pipes (particularly highly curved ones) under laminar flow conditions. The packing density (i.e. interfacial area) of these geometries is evaluated using a CAD software. The results reveal that HCHPs not only allow achieving much higher transfer rates than straight and classical helical pipes, but they can also be densely packed. Therefore, when appropriate designs are selected, impressive process intensification factors are achievable, with up to 8-fold volume reductions.

Finally, correlations are developed for evaluating the interfacial area and the heat/mass transfer efficiency in classical and highly curved helical pipes. In future works, these correlations will be used in model-based optimization for determining the optimal designs of helically coiled heat/mass exchangers.

Keywords: CFD; Correlation; Heat transfer; Helical pipe; Mass transfer; Packing density

1. Introduction

Economic issues and continuously strengthening environmental regulations force the industry to develop increasingly compact reactors and heat and mass transfer equipment. Such units allow improving the processes efficiency while reducing their overall energy requirements, costs, environmental impacts, weight and footprint. More specifically, minimizing volume and/or weight is of primary importance in applications where space is limited, e.g. decentralized energy production, domestic applications, space and offshore processes.

Various strategies to enhance heat and mass transfer efficiencies have been proposed and employed [1, 2]. They include the use of rotating devices [3], pulsating flow [4], twisted tape inserts [5], vortex generators [6] or helical pipes, etc. Compared to other alternatives, helical pipes present the advantage of not involving any internals or moving parts. Therefore, they are less subject to failure, breakdown, fouling and clogging, and thus, require lower maintenance costs.

Compared to straight tubes, due to centrifugal effects, the flow in curved and helical pipes develops secondary flow structures called Dean cells (Figure 1). They consist in a pair of counter-rotating vortices in the cross-stream direction, perpendicularly to the primary flow. These vortices allow a great improvement of the transfer efficiency. Indeed, if we consider fully developed laminar flow conditions, in the case of straight tubes, fluid particles move along straight streamlines parallel to the walls. Therefore, lateral mixing, i.e. radial heat/mass transfer, occurs under the sole effect of conduction/diffusion, which leads to poor transfer efficiencies when the pipe diameter is not too small. On the other hand, in helical pipes, Dean cells provide efficient advective transport of the fluid particles between the pipe walls and its centerline, leading to increased transfer performance. Accordingly, these geometries have been suggested and/or employed in several applications and industrial processes: (1) Heat transfer enhancement for nuclear plants [7] and many other applications [8, 9]. (2) Increased mass transfer rates in catalytic reactors [10], dense [11] and porous [2] membrane contactors, etc. (3) Improvement of mixing efficiency [12].

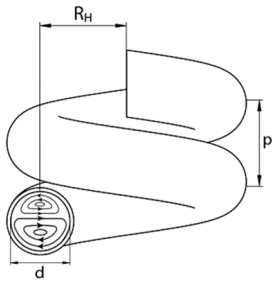

Figure 1: Schematic representation of Dean cells in a helical pipe.

The shape of a helical pipe is described by two geometric parameters, the dimensionless pitch, $p^* = p/d$, and the dimensionless helix radius, $R_H^* = R_H/d$, where d is the pipe diameter, p the helix pitch and R_H the helix radius. Figure 2 illustrates some representative helical tube geometries and the limits of the so-called forbidden region. The equation of this frontier has been determined by Przybył and Pierański [13]: it corresponds to the limit beyond which it is not possible to further decrease the helix pitch because the consecutive turns of the helix would overlap one with another. In other terms, the forbidden region corresponds to the set of p^* and R_H^* for which it is no more possible to design helical shapes. Figure 3 is a contour plot of the dimensionless helix curvature, $\kappa^* = \kappa\, d = d/\gamma$, in the (R_H^*, p^*) space, where κ is the pipe curvature and γ its curvature radius. The mathematical expression of κ is as follows:

$$\kappa = \frac{1}{R_H\left[1 + \left(\frac{p}{2\pi R_H}\right)^2\right]} \qquad \text{Eq. 1}$$

Figure 3 illustrates the fact that the helix curvature tends toward zero at three asymptotic limits: (1) when the dimensionless pitch, $p^* = p/d$, tends to infinity. (2) when the dimensionless helix radius $R_H^* = R_H/d$ tends to zero. (3) when R_H^* tends to infinity. Indeed, as shown in Figure 2, at the first two limits, the helix geometry tends toward that of a straight tube, while at the third limit, the helical tube straightens and becomes locally similar to a straight pipe.

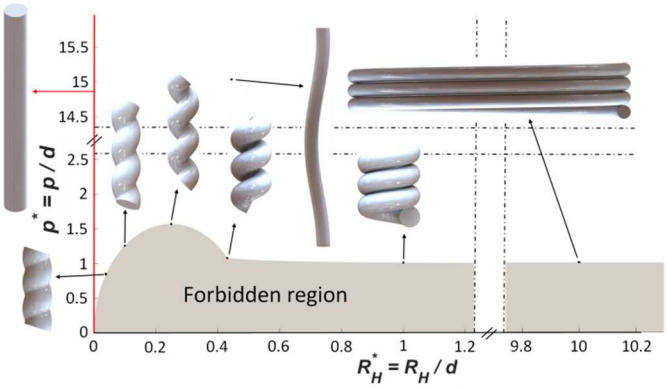

Figure 2: Limit of the forbidden region in the (R_H^*, p^*) space (adapted from [13]) and some representative helix geometries [14].

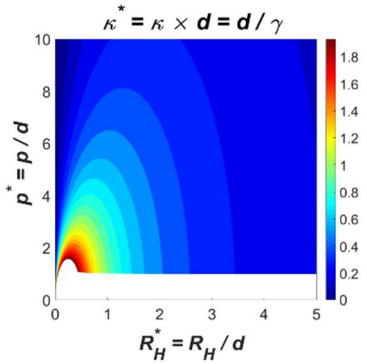

Figure 3: Contour plot of the dimensionless helix curvature in the (R_H^*, p^*) space.

Most importantly, Figure 3 reveals that the highest pipe curvatures are associated to helixes of low pitch and relatively low helical radius. These geometries will be referred to as Highly Curved Helical Pipes (HCHPs) further on in this paper. Given their low radius of curvature, they exhibit the highest centrifugal effects. Thus, HCHPs are expected to produce the most intense Dean vortices, which should lead to the best heat/mass transfer performance. Nonetheless, to the authors' best knowledge, no previous study has focused yet on the transfer efficiency in such geometries. As can be noticed from Table 1 for example, only 'classical' helical geometries have been considered thus far in literature. This is probably because HCHPs are difficult to fabricate using traditional manufacturing techniques.

Studies dealing with classical helical pipes have shown that these geometries allow a significant enhancement of the heat/mass transfer. Indeed, Nusselt and Sherwood numbers up to 7 times greater than in straight tubes were reported in literature [19, 24, 25]. However, it is noteworthy that helical pipes cannot be as densely packed as straight ones. Therefore, the transfer efficiency improvement they allow is - at least partially - counterbalanced by their lower packing density. For example, Kaufhold et al. [26] reported that if R_H^* is not sufficiently small, classical helixes lead to lower performance than straight tubes in terms of volumetric mass transfer rates (i.e. mass flux per unit volume).

Interestingly, HCHPs are not only expected to lead to better transfer rates than classical helixes, but also, their elongated shape (Figure 2) allow them to be densely packed. Hence they should allow a significant intensification of the overall transfer rate, i.e. a meaningful unit volume reduction of reactors, heat exchangers and membrane contactors. Nowadays, with the development of 3D-printing technologies, manufacturing HCHPs has become achievable [14]. Therefore, investigating their performance in terms of heat and mass transfer efficiency offers significant interest from both academic and industrial points of view.

This paper focuses on transport phenomena in helical pipes, particularly highly curved ones (HCHPs), under fully developed laminar flow conditions. The laminar flow regime is encountered in many applications of practical interest, in particular small-scale devices, e.g. microfluidics, micro-structured heat exchangers and reactors, micro-mixers and hollow fiber membranes. CFD (computational fluid dynamics) simulations are reported hereafter in order to determine the Nusselt number in helical pipes, and by analogy, the Sherwood number. Different operating conditions, described by the Reynolds number, and various helix designs are examined. Prandtl numbers (and by analogy, Schmidt numbers) ranging from 1 to 10 are considered. This range of fluid properties covers many existing processes. Additionally, for evaluating the volumetric transfer rates allowed, helixes packing density as a function of the helixes geometry has been determined using a CAD (computer-aided design) software.

CFD results revealed that among helical pipes, highly curved ones allow achieving the maximal Nusselt and Sherwood numbers, which can be nearly an order of magnitude higher than in straight ones. Moreover, numerical data confirmed that HCHPs can be densely packed. The volumetric transfer rates they allow is up to 8 times higher than that reached with straight tubes. On the other hand, given their low packing densities, classical helical pipes may lead to lower overall performance than straight ones.

It is also shown that available correlations fail in estimating the heat/mass transfer rates in HCHPs and the helixes packing density with a sufficient accuracy. Therefore, two new correlations are proposed in this paper. The first one allows predicting the Nusselt and Sherwood numbers over a wide range of helical pipe geometries and operating condition, and the second allows determining the optimal packing density as a function of the helix geometry. This set of correlations, along with that proposed by Abushammala et al. [14] for calculating the friction coefficient in helical pipes, can be used in model-based optimization of helically coiled heat exchangers / membrane contactors. This procedure allows determining the optimal helix geometry, i.e. the one leading to the most lucrative trade-off between the process intensification (unit volume reduction) and energy efficiency (extra pressure drop).

2. CFD computation of Nusselt (and Sherwood) number in helical pipe flows

Table 1: Set of commonly used correlations for predicting Nu_H^∞ and Sh_H^∞ for laminar flow in helical pipes under uniform wall temperature/concentration. Nu_H^∞ and Sh_H^∞ respectively correspond to the asymptotic Nusselt and Sherwood numbers in helical pipes.

Reference	Correlation	Correlation's validity range according to its authors	Geometric parameters of the helical pipes investigated
Schmidt [15]	$Nu_H^\infty = 3.65 + 0.08\left[1 + 0.8\left(\frac{1}{2R_H^*}\right)^{0.9}\right] Pr^{\frac{1}{3}}\, Re^m$ $m = 0.5 + 0.2903\left(\frac{1}{2R_H^*}\right)^{0.194}$	Laminar regime with $Re \geq 100$ Large range of Pr (air, water and oil were used as test fluids)	$2.5 \leq R_H^* \leq 42$ $3 \leq p^* \leq 137$
Dravid et al. [16]	$Nu_H^\infty = (0.76 + 0.65 {De_{R_H}}^{0.5}) Pr^{0.175}$	$50 \leq De_{R_H} \leq 2\,000$ $5 \leq Pr \leq 175$	$10 \leq R_H^* \leq 50$ The range of p^* is not reported.
Kalb and Seader [17]	$Nu_H^\infty = 0.836\, De_{R_H}^{0.5}\; Pr^{0.1}$	$De_{R_H} \geq 80$ $0.7 \leq Pr \leq 5$	$5 \leq R_H^* \leq 50$ The range of p^* is not reported.
Manlapaz and Churchill [18]	$Nu_H^\infty = \left[\left(3.657 + \frac{4.343}{z_1}\right)^3 + 1.158\left(\frac{De_{R_H}}{z_2}\right)^{3/2}\right]^{1/3}$ $z_1 = (1 + \frac{957}{{De_{R_H}}^2\, Pr})^2 \;;\; z_2 = 1 + \frac{0.477}{Pr}$	Entire laminar regime	$R_H^* \geq 2.5$ The range of p^* is not reported.
Moulin et al. [19]	$Sh_H^\infty = 0.14\, {De_\gamma}^{0.75}\, Sc^{0.33}$	$150 \leq Re \leq 2\,000$	$11.5 \leq R_H^* \leq 12.4$ $9.9 \leq p^* \leq 15.4$
Yildiz et al. [20]	$Nu_H^\infty = 0.0551\, De_{R_H}^{0.864}\; Pr^{0.4}$	$1\,265 \leq De_{R_H} \leq 2\,000$ $5 \leq Pr \leq 175$	$120 \leq p^* \leq 360$ $R_H^* = 7.5$
Xin and Ebadion [21]	$Nu_H^\infty = (0.318 De_{R_H}^{0.643} + 2.153) Pr^{0.177}$	$20 \leq De_{R_H} \leq 2\,000$ $0.7 \leq Pr \leq 175$	$22.6 \leq R_H^* \leq 75$ The value of p^* was not reported.
Ghobadi and Muzychka [22]	$Nu_H^\infty = [3.66^4 + \left(0.91375\; {De_{R_H}}^{0.5}\; Pr^{-0.1}\right)^4]^{1/4}$	$40 \leq De_{R_H} \leq 700$ $5 \leq Pr \leq 15$	$6.1 \leq R_H^* \leq 24.2$ The range of p^* is not reported.
Sheeba et al. [23]	$Nu_H^\infty = 3.6063\, De_{R_H}^{0.2216}\, Pr^{0.0540}\, (\frac{p*}{2\pi R_H^*})^{0.0472}$	$200 \leq De_{R_H} \leq 700$	$R_H^* = 29.7$ $2 \leq p^* \leq 18.2$

2.1. Nusselt (and Sherwood) number in helical pipe flows

In helical and curved pipes undergoing heat transfer between the fluid flow and the wall, the convective heat transfer is not uniform over the wall, but varies in both radial and axial directions. However, in most engineering applications, only the heat transfer coefficient averaged over the pipe circumference (i.e. in the radial direction) is of practical interest. It will be simply referred to as convective heat transfer coefficient, h, in the remaining part of this paper.

Considering a cross-section of the tube, the fluid mixing-cup temperature (i.e. mass flow rate weighted temperature), $T_{f,MC}$, at this position is calculated as follows:

$$T_{f,MC} = \frac{\iint_S \rho\, T\, \vec{\boldsymbol{u}}.\vec{\boldsymbol{n}}\, dS}{\iint_S \rho\, \vec{\boldsymbol{u}}.\vec{\boldsymbol{n}}\, dS} = \frac{\iint_S \rho\, T\, \vec{\boldsymbol{u}}.\vec{\boldsymbol{n}}\, dS}{\dot{m}} \qquad \text{Eq. 2}$$

where S is the surface of the circular flow section (Figure 4) and $\vec{\boldsymbol{n}}$ its unit normal vector. ρ denotes the fluid density, T the local fluid temperature, $\vec{\boldsymbol{u}}$ its velocity and $\dot{m}$ its total mass flow rate. The convective heat transfer coefficient at this position is defined and can be calculated as follows:

$$h = \lim_{S_w \to 0} \frac{\Phi}{S_w \left(T_w - T_{f,MC}\right)} \qquad \text{Eq. 3}$$

where S_w is an annular surface on the wall (Figure 4) inclosing the flow section, S. T_w is the average temperature of this wall element, or simply the wall temperature when an isothermal wall is considered as in this paper. Φ denotes the heat flux transferred between the wall element and the flow. The Nusselt number, Nu, which can be regarded as a dimensionless expression of h, is defined as follows in both helical and straight pipes:

$$Nu = \frac{h\, d}{\lambda} \qquad \text{Eq. 4}$$

where d is the pipe internal diameter and λ the fluid thermal conductivity.

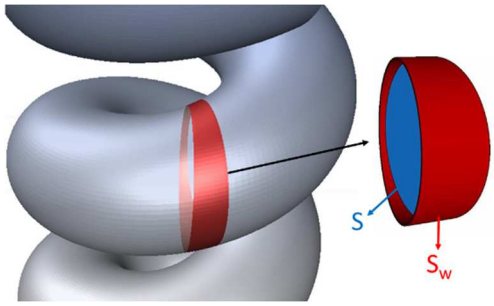

Figure 4: Typical shape of a wall element (in red) over which h *is* averaged.

Figure 5a illustrates a qualitative variation of Nu (and thus of h) along a helical or a straight tube, the abscissa axis being the - curvilinear - position along the pipe centerline. The Nusselt number is the highest at the pipe entrance and decreases over a distance called 'thermal entrance length' before reaching an asymptotic value, Nu^{∞}. For a laminar flow in a straight pipe under uniform wall temperature conditions, the length of the thermal entrance region, L_{th}, can be estimated as follows [27]:

$$L_{th} = Maximum\,(0.0565\, Re\, d\,;\, 0.037\, Re \Pr d) \qquad \text{Eq. 5}$$

$Re = Ud/\nu$ is the Reynolds number, where U is the mean velocity of the primary flow and ν the fluid kinematic viscosity, $Pr = \nu/\alpha$ is the Prandtl number where α is the fluid thermal diffusivity. The first term on the right hand side of Eq. 5 represents the length required for the flow to fully develop, i.e. for the velocity field and the local friction factor to become axially invariant, while the second term corresponds to the distance required for the flow to become thermally developed.

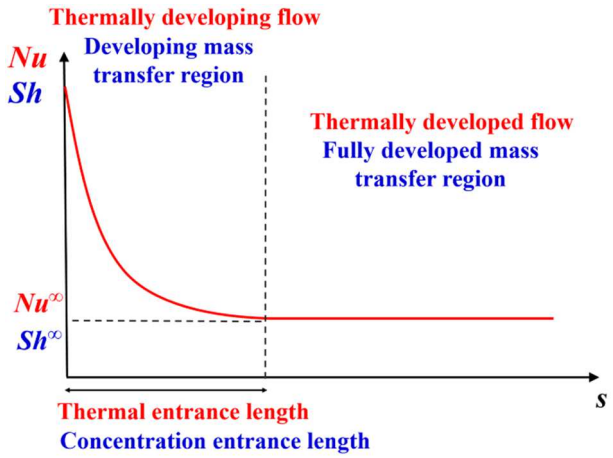

Figure 5: Typical variation of the Nusselt (Sherwood) number from the entrance of a straight or a helical pipe.

Equation 5 reveals that the thermal entrance length may become very important for large values of *Pr*. However, in the current study, only *Pr* numbers ranging from 1 to 10 are considered. With such fluids, entrance effects are usually negligible in the case of pipes of small diameter and/or sufficient length, which is generally the case in the applications targeted in this study, namely heat exchangers (and catalytic reactors and hollow fiber membranes in the case of mass transfer). This is particularly true when dealing with helical geometries. Indeed, under similar operating conditions, the entrance length in helical pipes is generally shorter than in straight ones [28]. Therefore, the asymptotic Nusselt number, Nu^{∞}, is sufficient for characterizing the effective heat transfer in helical shape exchangers. Accordingly, in this paper, determination of Nu^{∞} in helical pipes via CFD simulations will be emphasized. Thus, although the flow and heat transfer characteristics over the entire pipe are simulated, only Nu^{∞} results are reported; entrance effects data are considered beyond the scope of this paper and will not be reported here.

With a laminar flow regime and an isothermal wall, under ideal conditions (see Section 2.2), the asymptotic Nusselt number in straight pipes, Nu_S^{∞}, equals 3.657 [29]. On the other hand, contrary to Nu_S^{∞}, the asymptotic Nusselt number in helical pipes, Nu_H^{∞}, is not constant, but depends on both Reynolds and Prandtl numbers as well as on the pipe geometry.

Assuming an incompressible flow with uniform fluid properties, the heat transfer coefficient under thermally developed flow conditions would depend on the helical pipe geometric parameters (d, R_H and p), the fluid properties (ρ, ν, λ and α) and the mean velocity of the primary flow, U. Therefore, according to the Buckingham π theorem, Nu_H^{∞} is a functional relation of the following four independent dimensionless parameters: (1) The dimensionless helix pitch, $p^* = p/d$. (2) The dimensionless helix radius, $R_H^* = R_H/d$. These first two parameters characterize the helix shape. (3) The Reynolds number, $Re = Ud/\nu$, which accounts for the operating conditions. (4) The Prandtl number, *Pr*, which accounts for the fluid properties. As a result of the heat transfer enhancement by the Dean vortices, Nu_H^{∞} is always greater than 3.657. Table 1 shows a summary of commonly used correlations for evaluating Nu_H^{∞} under laminar flow conditions.

Finally, it is worthy to note that the heat transfer analysis carried out in this section can be transposed and applied to mass transfer phenomena. In fact, it has been long recognized that heat and mass transfer processes present similar behaviours. Indeed, in many practical situations, the equations describing mass and heat transfer are mathematically analogous (see Sections 2.2 and 2.3 for details). Accordingly, heat transfer results can be converted to mass transfer results and vice versa.

Hence, in the framework of the present study, the heat/mass analogy stipulates that if the same geometric (R_H^* and p^*) and operating conditions (Re) are considered, then:

$$Sh_H^{\infty} = Nu_H^{\infty} \ \ (and\ Sh = Nu) \quad if \quad Sc = Pr \qquad \text{Eq. 6}$$

where Sh is the Sherwood number (the mass transfer analogue to Nu) and Sh_H^{∞} its asymptotic value in helical pipes. Sh is defined as follows:

$$Sh = \frac{k\,d}{D} \qquad \text{Eq. 7}$$

where k is the convective mass transfer coefficient between the wall and the fluid and D the mass diffusivity of the involved species. Under laminar flow conditions and uniform wall concentration, Sh_H^{∞} equals 3.657 in virtue

of the heat/mass transfer analogy. $Sc = \nu/D$ is the Schmidt number, the mass transfer analogue of Pr. It represents the ratio of momentum diffusivity (kinematic viscosity) to mass diffusivity. Based on the above discussion about Nu_H^∞ and the heat/mass transfer analogy, it can be argued that Sh_H^∞ depends on the following four dimensionless numbers: R_H^*, p^*, Re and Sc.

2.2. CFD modeling and simulation of heat transfer in helical pipes under laminar flow conditions

CFD simulations were carried out for various helical pipe designs and operating conditions. The geometries were drawn using Autodesk Inventor Professional 2018 software, based on a sufficient tube length to attain the thermally developed flow region. The 3D numerical domain was meshed using the ANSYS Meshing software. The grid consisted of hexahedral cells only, with a boundary layer mesh in the near-wall region for an accurate calculation of the steep gradients prevailing in this zone. Based on preliminary simulations, the cells size and density were chosen so at to ensure a mesh-independent solution for all the cases studied.

CFD simulations were conducted using the commercial code ANSYS Fluent 16. The flow field in the pipe was determined by solving the continuity and Navier-Stokes equations assuming a Newtonian, incompressible, and steady flow and uniform fluid properties (density and viscosity):

$$div(\vec{\boldsymbol{u}}) = 0$$

$$\overrightarrow{\boldsymbol{div}}(\vec{\boldsymbol{u}} \otimes \vec{\boldsymbol{u}}) = -\frac{1}{\rho}\vec{\boldsymbol{\nabla}}P + \nu\,\vec{\Delta}\vec{\boldsymbol{u}} \qquad \text{Eqs. 8}$$

As boundary conditions, a uniform velocity profile was set at the pipe inlet: as the flow rate is imposed and since a uniform fluid density is considered, the gravity force has no effect on the velocity field and therefore this body force term was not included in the Navier-Stokes equations. At the pipe outlet, a uniform pressure condition was used and the no-slip condition was set at the pipe wall.

The temperature field was determined by solving the energy balance equation:

$$div(\vec{\boldsymbol{u}}\,T) = \alpha\,\Delta T \qquad \text{Eq. 9}$$

As boundary conditions, a uniform fluid temperature is enforced at the inlet, an isothermal wall is considered and the zero temperature gradient is imposed at the pipe outlet. It is noteworthy that the velocity and temperature profiles at the inlet affect the flow and heat transfer phenomena in the entrance region only. Therefore, as this paper focuses on heat transfer in the thermally developed zone (i.e. Nu_H^∞), the velocity and temperature distributions at the inlet were simply considered as uniform.

The CFD model (i.e. Equations 8 and 9 and their boundary conditions) assumes: (1) Steady-state flow and heat transfer phenomena. (2) An incompressible Newtonian fluid with uniform properties. (3) The absence of phase transition phenomena. (4) A purely forced convection. Indeed, natural convection effects are neglected since the fluid density is supposed uniform. This assumption is relevant as long as the Reynolds number is not extremely low and the Grashof number (i.e. buoyancy effects) not extremely high, which is generally the case in heat exchangers. (5) Radiative phenomena are ignored. (6) Heat generation by viscous dissipation is neglected in Equation 9. This hypothesis is relevant apart in few particular situations where highly viscous fluids are used under high strain rate conditions. It is worthy to note that, if in addition the axial heat conduction effects are neglected, these assumptions lead to the theoretical result of $Nu_S^\infty = 3.657$ in the case of straight pipes [29].

The hydrodynamics and heat equations were iteratively solved until convergence. The advective terms were discretized using the QUICK scheme while the diffusive ones were central-differenced. Pressure interpolation was carried out using a second order scheme.

A total of nearly 280 CFD simulations was carried out. More than 25 helix designs (particularly highly curved ones) were investigated within the following range of geometric conditions: $1.25 \leq p^* \leq 15$ and $0.05 \leq R_H^* \leq 10$. Eight Reynolds number values, ranging from 10 to 2 000, were examined. Three Prandtl numbers were considered in the simulations: 1, 5 and 10. Fluids used in many industrial applications fall within this range of Pr, e.g. most gases, water, refrigerants, many light organic liquids, molten salts and some oils under very high temperature conditions.

For each simulation, the local Nu was calculated at different longitudinal positions across the pipe length using Equations 3 and 4 (and considering a sufficiently small wall element as that depicted on Figure 4), and its asymptotic value, Nu_H^∞, was determined. These CFD results were used to correlate Nu_H^∞ as a function of the helix design (p^* and R_H^*), the fluid properties (Pr) and the flow conditions (Re). They are provided in an Excel sheet as supplementary material to this paper.

2.3. Heat and mass transfer analogy

The procedure described in Section 2.2 allows determining the Nusselt number characterizing the heat transfer between the fluid and the pipe wall for *Pr* ranging from 1 to 10. Under some conditions discussed thereafter, the obtained results may be transposed to describe mass transfer between the fluid and the wall (e.g. mass transfer in membranes, adsorption or heterogeneous reaction processes). Obviously, this is possible for Schmidt numbers in the range of 1 to 10, which is the case in most gas-gas systems.

In binary mixtures with uniform density, the diffusive mass flux of a component A, $\vec{\boldsymbol{n}}_{\boldsymbol{A}}$ (in kg m^{-2} s^{-1}), is given by Fick's law:

$$\vec{\boldsymbol{n}}_{\boldsymbol{A}} = -D\ \overrightarrow{\boldsymbol{grad}}(\rho_A) + \rho_A \vec{\boldsymbol{v}} \qquad \text{Eq. 10}$$

where ρ_A is the mass concentration of A and D its mass diffusivity. $\vec{\boldsymbol{v}}$ is the velocity resulting from the diffusive motion of A and the other species within the mixture. The second term on the right-hand side of Eq.10 is generally referred to as the 'bulk motion contribution'. It represents the advective mass flux resulting from the diffusion of the different species which induces a local motion of the mixture. When this term is negligible, Fick's law becomes analogue to Fourier's law of heat conduction. This is the case under equimolar counter diffusion of species of similar molecular weights or under dilute mixture conditions. Such conditions are encountered in many important gas-gas applications such as tritium removal, recovery of volatile organic compounds and adsorption processes in isotropic mixtures, etc. Most importantly, the bulk motion contribution can be generally neglected in forced convection situations when the Reynolds number is not very low and the flow field three-dimensional (as in the presence of Dean vortices). This significantly broadens the range of conditions for which the heat/mass transfer analogy can be applied in helical geometries.

When the bulk motion contribution is negligible, in the absence of any homogeneous chemical reaction, if uniform fluid properties are considered, the steady-state the mass transfer equation becomes analogue to Eq. 9 and is given by:

$$div(\vec{\boldsymbol{u}}\ C_A) = D\ \Delta C_A \qquad \text{Eq. 11}$$

where C_A is the molar concentration of component A.

Another restriction to the validity of the heat/mass transfer analogy concerns the boundary condition at the wall. Indeed, in heat transfer simulations (Section 2.2), the no-slip condition applies at the pipe wall, while in mass transfer processes, the mass flux at the wall obviously results in a non-zero wall-normal velocity. However, in many situations, this velocity component has negligible effects on the flow field, and thus, the heat/mass transfer analogy remains valid. This is the case in equimolar counter diffusion of species of similar molecular weights or under dilute mixture conditions, even in the presence of a heterogeneous reaction or adsorption phenomena at the wall. In any case, in situations where the heat/mass transfer analogy is not strictly valid, although the results reported in this paper do not allow a precise evaluation of the Sherwood number, they still provide a first insight about the optimal shape of helical tubes in mass transfer devices.

3. Optimal packing density of helixes

Helical pipes allow higher transfer efficiencies per unit surface than straight ones. However, they cannot be as densely packed as straight tubes. Thus, the transfer efficiency improvement they provide can be - at least partially - counterbalanced by their lower packing density. Therefore, in order to determine the overall volumetric transfer rate (i.e. heat/mass flux per unit volume) that helical pipes allow achieving, it is necessary to calculate their optimal packing density. To the authors' best knowledge, no analytical solution for this problem has been published thus far in literature. Only Kaufhold et al. [26] have reported a correlation for estimating helixes packing density, however, as discussed in Section 4.5, their model is highly inaccurate.

The ideal arrangement for non-overlapping straight tubes or cylinders is an - equilateral - triangular packing (also known as dense hexagonal lattice) (Figure 6a) where the distance between the axes of two neighboring cylinders equals their diameter. This configuration allows the straight tubes to best cover the available volume: it can been analytically shown that, $\phi_{S,max}$, the volume fraction they fill, equals $\pi/[4\ \sin(\pi/3)] \approx 90.7\%$.

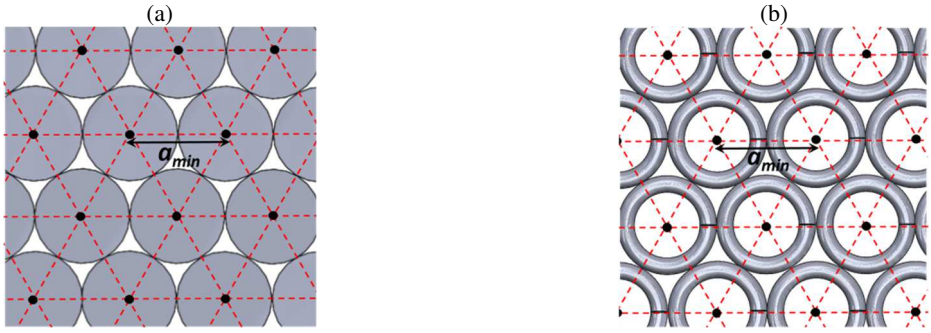

Figure 6: Top view of: (a) ideally packed cylinders. (b) ideally packed helixes of R_H^* = 2.5 and p^* = 1.25. The triangular (or dense hexagonal) lattice is illustrated by dashed lines. The black dots represent the axes of the helical or straight tubes.

The CAD commercial software Autodesk Inventor Professional 2018 was used for determining the ideal packing of identical helixes under a triangular arrangement. a_{min} will denote the minimum achievable distance between two neighboring non-overlapping helixes (Figure 6b) and $\phi_{H,max}$ the volume fraction occupied by these closely packed helixes.

a_{min} was determined for more than 240 helix designs in the following range of geometric conditions: $1 \leq p^* \leq 20$ and $0.05 \leq R_H^* \leq 10$. Given the periodicity of the lattice, only three helixes disposed on an equilateral triangular pattern were drawn using the CAD software. Their diameter, *d,* was arbitrarily taken as 1 mm. The distance separating these helixes was iteratively decreased until determining a_{min} with an absolute tolerance of 0.01 mm. As the lowest possible value for a_{min} is the pipe diameter (situation that occurs in the case of straight pipes), i.e. 1 mm in the present case, thus, the maximum relative error on the computed a_{min} values is about 1%.

These results allowed calculating, $a_{min}^* = a_{min}/d$, the dimensionless minimum distance separating the closely packed helixes. Indeed, dimensionless analysis shows that a_{min}^* is a functional relation of $p^*$and R_H^*. The CAD results were used to correlate a_{min}^* as a function of these two geometric parameters. They are provided in an Excel sheet as supplementary material to this paper.

For a given helix design, once the a_{min}^* value is known, $\phi_{H,max}$ can be easily calculated. Indeed, let's consider a triangular prism of height equal to *p*, the pitch of the helix, and which base is the equilateral triangle that connects the axes of the three closely packed helixes. This volume encloses 1/6th of each of the three helices, which corresponds to the volume of half a helix. Thus, $\phi_{H,max}$ equals to the half volume of a helix over the volume of the prism element:

$$\phi_{H,max} = \frac{\frac{1}{2} V_{Helix}}{V_{Prism}} = \frac{\frac{1}{2}\frac{\pi d^2}{4}\sqrt{p^2 + (2\pi R_H)^2}}{\frac{1}{2} a_{min}^2 \sin\left(\frac{\pi}{3}\right) p} = \frac{\pi \sqrt{1 + (2\pi R_H^*/p^*)^2}}{4\, a_{min}^{*2} \sin\left(\frac{\pi}{3}\right)} \quad \text{Eq. 12}$$

4. Results and discussion

4.1. CFD results

In the following sections, the CFD results will be mainly presented in terms of Nusselt number and heat transfer enhancement. However, as discussed in Section 2.3, based on the heat/mass transfer analogy, these same results can be interpreted in terms of Sherwood number and mass transfer enhancement.

As mentioned earlier, for each CFD simulation performed, the circumference-averaged *Nu* was calculated at different positions along the helical pipe length so as to determine its asymptotic value, Nu_H^∞. This value, divided by the Nusselt number in a straight pipe, Nu_S^∞ = 3.657, represents the heat transfer enhancement allowed by a given helical pipe.

Figure 7 shows contour plots of the Nu_H^∞ to Nu_S^∞ ratio in the (R_H^* , p^*) space. These contours were obtained using a triangulation-based cubic interpolation of the CFD results. The geometric parameters for which simulations were performed are represented by black dots. It is worthy to note that, at these points, the values of Nu_H^∞ (divided by Nu_S^∞) that are displayed on the contour plots are exactly the same than those provided by CFD. On the other hand, the results predicted between these points are generated by interpolation. Therefore, they may be expected to not be very accurate since they are quite sensitive to the interpolation scheme used. Indeed, as can be noticed from Figure 7, the contour plots exhibit some relatively irregular variations.

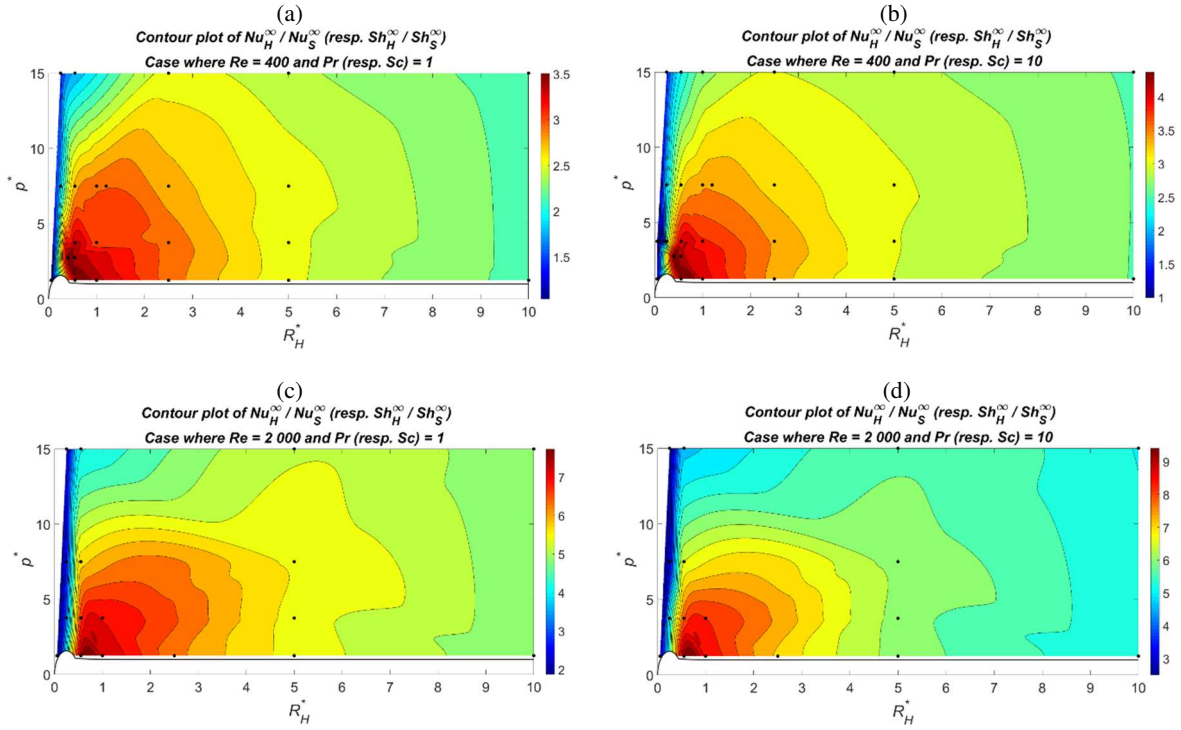

Figure 7: Contour plots of the Nu_H^∞ to Nu_S^∞ (respectively Sh_H^∞ to Sh_S^∞) ratio at: (a) Re = 400 and Pr (resp. Sc) = 1. (b) Re = 400 and Pr (resp. Sc) = 10. (c) Re = 2 000 and Pr (resp. Sc) = 1. (d) Re = 2 000 and Pr (resp. Sc) = 10. The black dots represent the geometric conditions for which CFD simulations have been performed. The contours are derived by interpolating these data.

Nonetheless, these contours allow deriving several major conclusions:

(1) HCHPs allow a great improvement of the heat transfer efficiency compared to straight tubes. Indeed, given their high curvatures (Figure 3), the flow in HCHPs undergoes strong centrifugal effects leading to intense Dean-type vortices that greatly improve the heat transfer rates.

(2) As Re increases, centrifugal forces become more intense, which further enhances the heat transfer efficiency. Hence, in the case where Pr = 1, for Re = 400, the maximal Nu_H^∞ achieved in HCHPs is about 3.5 times higher than in straight tubes (Figure 7a), and its gets nearly 8 times greater than Nu_S^∞ for Re = 2 000 (Figure 7c).

(3) Nu_H^∞ increases when Pr is increased. For example, under a Re of 2 000, the maximal Nu_H^∞ is about 8 times higher than in straight tubes for Pr = 1 (Figure 7c), and becomes more than 9 times greater than Nu_S^∞ for Pr = 10 (Figure 7d).

(4) The geometric parameters for which Nu_H^∞ is maximal are not significantly affected by the Reynolds and Prandtl numbers values. However, when Re and/or Pr are increased, the value of Nu_H^∞ becomes more sensitive to the helix geometry.

(5) For any given dimensionless pitch, p^*, there exists an optimal dimensionless helix radius, R_H^*, at which Nu_H^∞ is maximal. The Nu_H^∞ to Nu_S^∞ ratio sharply decreases toward unity when R_H^* tends to zero as the helix geometry approaches that of a straight pipe. This ratio also decreases to unity when R_H^* tends to infinity as the helical pipe straightens (its curvature tends to zero as can be seen from Figure 3) and becomes locally similar to a straight tube. However, these effects are not always clearly noticeable from the contour plots of Figure 7 since simulations were performed in the range of $0.05 \leq R_H^* \leq 10$ only.

(6) For any given R_H^*, the Nu_H^∞ to Nu_S^∞ ratio decreases when p^* increases and tends towards unity at infinite p^* as the helix design approaches a straight pipe, although this effect is not always noticeable in Figure 7 as no simulations were performed for p^* values higher than 15.

(7) Although Nu_H^∞ decreases when p^* is increased, as can be seen from Figure 7, this effect is only significant in the case of HCHPs. Indeed, for relatively high R_H^* values, the curvature is not much sensitive to the value of p^* (Figure 3). As only helical pipes with rather large R_H^* were investigated in the literature, most authors concluded that the helix pitch has no significant effect on Nu_H^∞ as can be noticed from the correlations reported in Table 1. Thus, it is obvious that these correlations cannot accurately predict the Nusselt number in HCHPs as detailed in Section 4.3.

4.2. Correlation for predicting Nusselt (and Sherwood) numbers in helical pipe laminar flows

The CFD results revealed that, for given Re and Pr numbers, the Nu_H^∞ field in the (R_H^* , p^*) space (Figure 7) presents a single maximum (no local optima). And apart the particular case of straight pipes, for any helix geometry, Nu_H^∞ increases with increasing Re and Pr.

Despite such a relatively regular behavior, finding a mathematical model that correctly fits the CFD data was extremely challenging and tedious. Indeed, Nu_H^∞ exhibits highly nonlinear variations, especially with respect to the geometric parameters. In fact, the Nu_H^∞ field undergoes steep variations in the HCHPs region, with highly non-uniform and anisotropic gradients, which magnitudes are very sensitive to the helix geometry. Moreover, the mathematical formulation should ensure that the model predicts that $Nu_H^\infty = Nu_S^\infty = 3.657$ at all of the three asymptotic limits where the pipe curvature vanishes and the helix geometry tends toward that of a straight tube, i.e. when R_H^* tends to zero or infinity and when p^* tends to infinity. Otherwise, the derived correlation cannot be reliably used in any model-based optimization for determining the optimal pipe design in heat/mass transfer devices.

The development of the regression model for fitting the Nu_H^∞ data has been conducted by trial-and-error. The following complex expression has been found to provide the best fit of the CFD results:

$$Nu_H^\infty = 3.657 + p_1\, A^{p_2}\, Re^B\, Pr^{p_7}\, exp(-C)$$

where:

$$A = \left[R_H^* \left(1 + \left(\frac{p^*}{2\pi R_H^{*p_3}}\right)^{p_4}\right)\right]^{-1} \qquad \text{Eqs. 13}$$

$$B = p_5\, Pr^{p_6}$$

$$C = p_8\, R_H^{*p_9}\, Pr^{p_{10}}$$

The present model includes 10 regression parameters denoted p_i (i being an integer ranging from 1 to 10) which values were determined using an optimization procedure. The term 3.657 corresponds to the asymptotic Nusselt number in a straight tube, Nu_S^∞. The second right-hand side term in the mathematical model is formulated so as to be always positive, hence, the present correlation guarantees that the predicted Nu_H^∞ value remains greater (or equal) than Nu_S^∞.

The term denoted A is analogous to the helix dimensionless curvature κ^* (see Eq. 1), with the difference that p_3 and p_4 are treated as optimization variables instead of assigning their values to 1 and 2 respectively. The term A vanishes when R_H^* tends to zero or infinity or when p^* tends to infinity, i.e. when the helical pipe geometry tends toward that of a straight one. Thus, the model correctly predicts that $Nu_H^\infty = Nu_S^\infty = 3.657$ at these three limits.

The mathematical expression presented in Equations 13 was used to correlate the CFD data. It should be recalled that, as mentioned in Section 2.2, these results were obtained in the following range of dimensionless parameters: $1.25 \le p^* \le 15$, $0.05 \le R_H^* \le 10$, $10 \le Re \le 2\,000$ and $1 \le Pr \le 10$. The optimization problem was formulated as a minimization of the maximum relative difference between the model predictions and the numerical data. For a better accuracy, two sets of parameter values were calculated, the first one for Re ranging from 10 to 400, and the second one for Re between 400 and 2 000. The optimal sets of parameters p_i are reported in Table 2. They were determined using a genetic algorithm and the results were further refined using a local optimizer, GRG2. An Excel sheet with the present correlation is available as supplementary material to this paper.

Table 2: Optimal sets for the parameters of the correlation expressed by Equations 13.

Validity range					
$10 \le Re \le 400$	$\boldsymbol{p_1}$	$\boldsymbol{p_2}$	$\boldsymbol{p_3}$	$\boldsymbol{p_4}$	$\boldsymbol{p_5}$
	3.73×10^{-2}	3.81×10^{-1}	9.50×10^{-1}	2.64	9.38×10^{-1}
	$\boldsymbol{p_6}$	$\boldsymbol{p_7}$	$\boldsymbol{p_8}$	$\boldsymbol{p_9}$	$\boldsymbol{p_{10}}$
	-7.09×10^{-2}	5.71×10^{-1}	6.43×10^{-2}	-1.15	3.84×10^{-1}
$400 \le Re \le 2\,000$	$\boldsymbol{p_1}$	$\boldsymbol{p_2}$	$\boldsymbol{p_3}$	$\boldsymbol{p_4}$	$\boldsymbol{p_5}$
	3.03×10^{-2}	2.82×10^{-1}	7.19×10^{-1}	2.62	5.7×10^{-1}
	$\boldsymbol{p_6}$	$\boldsymbol{p_7}$	$\boldsymbol{p_8}$	$\boldsymbol{p_9}$	$\boldsymbol{p_{10}}$
	-9.01×10^{-2}	4.35×10^{-1}	1.01×10^{-2}	-3.13	-1.32×10^{-1}

Figure 8 compares the correlation predictions and the present CFD results (represented by brown disks). It shows that the proposed correlation correctly fits the Nu_H^∞ data as most points are within an error margin of 15%. Indeed, the maximum relative difference between the numerical results and the correlation predictions is respectively 16.9% for *Re* below and 400 and 14.8% for *Re* above 400.

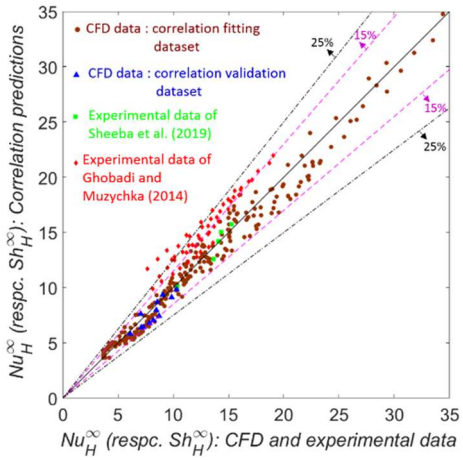

Figure 8: Parity diagram of Nu_H^∞: CFD and experimental data versus correlation predictions.

To check the robustness of the correlation, additional CFD simulations were performed for p^* up to 60 and R_H^* up to 20. Although the correlation was built upon CFD results acquired for $p^* \leq 15$ and $R_H^* \leq 10$, it successfully predicts these additional Nu_H^∞ data (represented by blue triangles in Figure 8) within an error margin below 15%. This predictive capacity of the present correlation is due to its mathematical formulation (Eqs. 13) which as discussed previously, guarantees correct results at the asymptotic limits where the helical pipe geometry tends toward that of a straight one, i.e. ensures results to be correctly bounded. Therefore, the present correlation is believed to lead to realistic and valid Nu_H^∞ values even beyond the range of geometric conditions investigated in this paper.

Figure 9 shows the contour plots of the Nu_H^∞ to Nu_S^∞ ratio that are calculated using the present correlation for *Re* values of 400 and 2 000 and *Pr* values of 1 and 10. A good agreement with Figure 7 is observed, although the model data are much smoother since they are not affected by interpolation approximations. The maximal values of Nu_H^∞ and the geometric parameters for which they occur are correctly estimated by the model, and the Nu_H^∞ variations with respect to the helix geometry, operating conditions and fluid properties are successfully predicted.

(a)

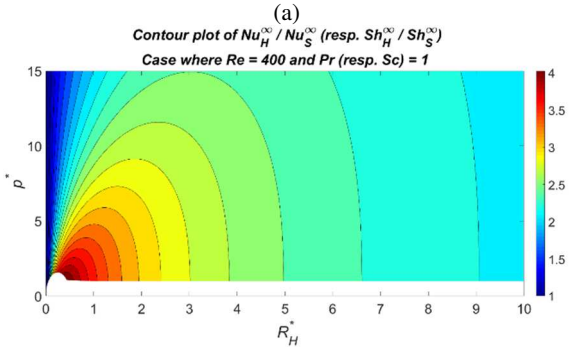

(b)

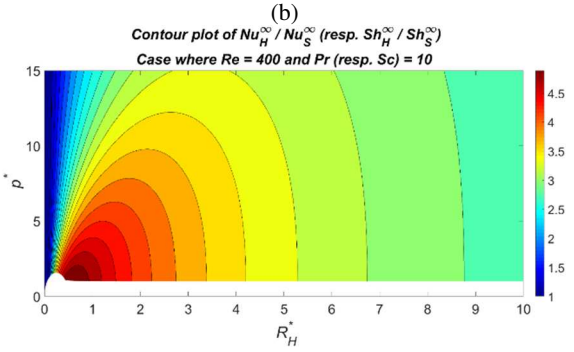

(c)

(d)

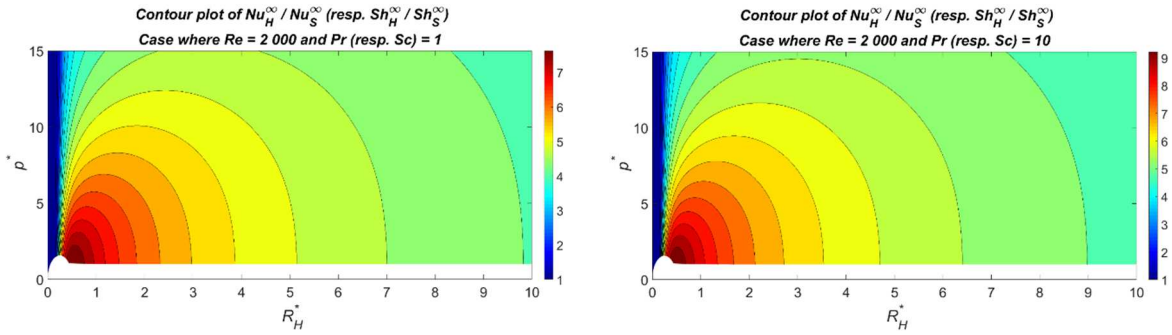

Figure 9: Contour plots of the Nu_H^∞ to Nu_S^∞ (respectively Sh_H^∞ to Sh_S^∞) ratio calculated using the present correlation (Eqs. 13): (a) Re = 400 and Pr (resp. Sc) = 1. (b) Re = 400 and Pr (resp. Sc) = 10. (c) Re = 2 000 and Pr (resp. Sc) = 1. (d) Re = 2 000 and Pr (resp. Sc) = 10. The contour plots at Re = 400 were generated using the set of parameters valid for $10 \leq Re \leq 400$ (Table 2).

4.3. Comparison between the current and literature correlations

In order to further assess the potentiality of the new correlation, its predictions are compared to that of literature correlations in Figures 10, 11 and 12. It is noteworthy that most available correlations (see Table 1) account for both flow and geometry effects via a single dimensionless parameter, the Dean number, which is defined as follows:

$$De_{R_H} = \frac{\rho d U}{\mu}\sqrt{\frac{d}{2R_H}} = Re\sqrt{\frac{1}{2R_H^*}} \qquad \text{Eq. 14}$$

However, this formulation leads to systematic errors in the HCHPs region. First, as shown in Figure 10 for the correlations of Dravid et al. [16] and Kalb and Seader [17], when R_H^* tends to zero, models based on De_{R_H} predict an infinite Nusselt number instead of 3.657. Moreover, these correlations ignore the effects of the helix pitch on the achieved Nu_H^∞. Indeed, as reported in Table 1, so far, literature studies has only dealt with 'classical helixes geometries', i.e. helical designs with a relatively high R_H^*. For such geometries, the helix pitch has little effect on Nu_H^∞ values as can been noticed from Figures 7 and 9, which explains why this parameter has not been considered in most previous correlations. Nonetheless, since these correlations were derived by regressing experimental measurements acquired on non-highly curved helixes, they are expected to accurately predict Nu_H^∞ in such geometries. Therefore, the good agreement between the current correlation and the former ones at large R_H^* values (Figure 9) validates the current CFD simulations and correlation for the case of classical helixes.

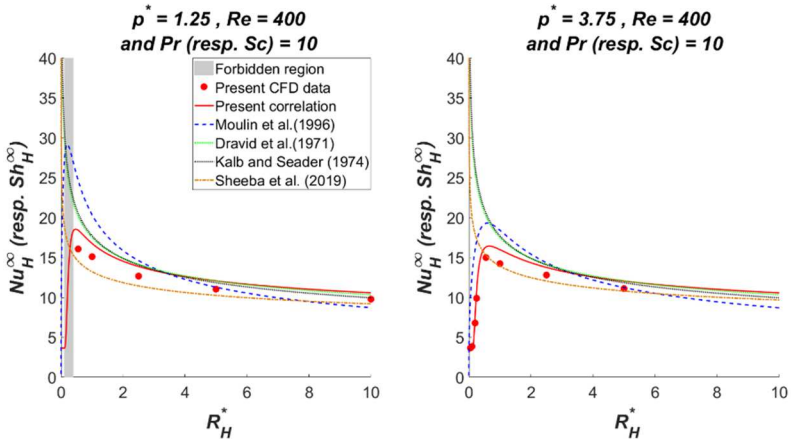

Figure 10: Nu_H^∞ (respectively Sh_H^∞) versus R_H^* at two different p^*: comparison of different correlations.

The correlation provided by Sheeba et al. [23] (Table 1) accounts for the helix pitch effects on the achieved Nu_H^∞. However, it presents two major weaknesses. First, it leads to an infinite Nusselt number when R_H^* tends to zero (Figure 10), and second, it predicts a slight increase of Nu_H^∞ when the helix pitch is increased (Figure 11) contrary to what is obtained by CFD and observed experimentally in other studies (e.g. [30]).

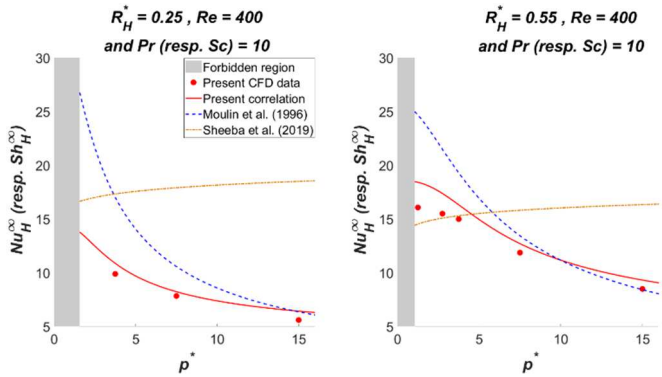

Figure 11: Nu_H^∞ (respectively Sh_H^∞) versus p^* at two different R_H^*: comparison between the present correlation and those of Moulin et al. [19] and Sheeba et al [23].

The correlation of Moulin et al. [19] (Table 1), built upon mass transfer experimental data, accounts for the helix geometry and operating conditions effects via a Dean number defined as follows:

$$De_\gamma = Re\sqrt{\frac{d}{2\gamma}} = Re\sqrt{\frac{\kappa^*}{2}} = Re\sqrt{\frac{1}{2R_H^*\left[1+\left(\frac{p^*}{2\pi R_H^*}\right)^2\right]}} \qquad \text{Eq. 15}$$

where κ^* is the dimensionless helix curvature. This definition of the Dean number is more appropriate than that presented in Eq. 14. In particular, De_γ vanishes at the three asymptotic limits for which the helix geometry approaches a straight pipe. This is why the correlation of Moulin et al. [19] correctly reproduces the shape of the curves showing Nu_H^∞ versus R_H^* (Figure 10) and captures the decrease of Nu_H^∞ when p^* is increased (Figure 11). However, it also suffers from several drawbacks. Indeed, it leads to Nu_H^∞ equal zero instead of 3.657 at the limits at which the helix curvature vanishes, i.e. when R_H^* tends to zero (Figure 10) or infinity and when p^* tends to infinity. More importantly, it largely overestimates the Nu_H^∞ value in HCHPs when *Re* is increased. As shown in Figure 12, the present model correctly captures the *Re* effects and is way more accurate than the correlation of Moulin et al. [19]. Note that the discontinuity in the actual correlation curves is due to the use of two different sets of parameter values depending on whether *Re* is higher or lower than 400 (Table 2).

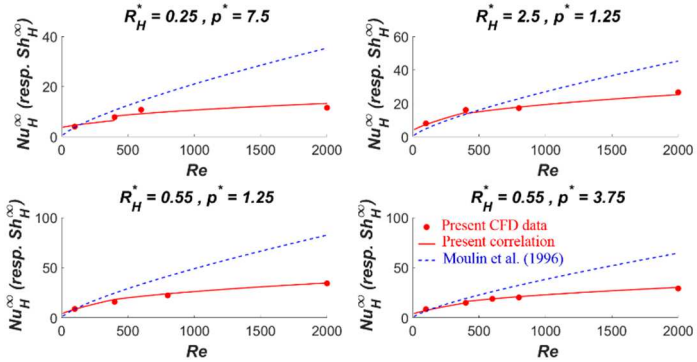

Figure 12: Nu_H^∞ (respectively Sh_H^∞) variation with *Re* for four different helixes at *Pr* (respectively *Sc*) = 10.

4.4. Correlation and CFD data validation using experimental data from literature

In addition to CFD results, for a more trustworthy validation, the correlation results were compared to the experimental data of Ghobadi and Muzychka [22] and Sheeba et al. [23]. Table 3 summarizes the geometric and operating conditions over which these measurements were obtained. It is noteworthy that even the experiments performed for a *Re* higher than 2 300 correspond to a laminar flow regime. Indeed, transition to turbulence is delayed in helical pipe flows due to the stabilizing effects of centrifugal forces [24, 31].

Table 3: Ranges of geometric and operating conditions over which the literature experimental data were acquired and the present correlation was built.

	Sheeba et al. [23]	Ghobadi and Muzychka [22]: helical pipe 1	Ghobadi and Muzychka [22]: helical pipe 2	Ghobadi and Muzychka [22]: helical pipe 3	Range of parameters investigated using CFD and upon which the present correlation was built
R_H^*	29.8	6.1	12.1	24.2	[0.05 – 10]
p^*	6.1	nearly 1	nearly 1	nearly 1	[1.25 – 15]
Pr	[3 – 5]	[5 – 8.5]	[5 – 8.5]	[5 – 8.5]	[1 – 10]
Re	[940 – 3 200]	[440 – 2 510]	[960 – 2 530]	[700 – 2 020]	[10 – 2 000]

The last column in Table 3 recalls the range of conditions over which the present CFD data were performed, and hence, upon which the current correlation was built. It can be noticed that most of the experimental results were acquired for conditions beyond the validity range of the present correlation. Nevertheless, as shown in Figures 8 and 13, an excellent agreement is obtained between the correlation and Sheeba et al. [23] results (represented by green squares) which were all predicted within an error margin of 9%. Figure 13 shows that the correlation correctly captures the effects of the Reynolds number. A good agreement is also obtained with the data of Ghobadi and Muzychka [22] (represented by red diamonds in Figure 8) as most of their experimental results are predicted with a relative error less than 25%.

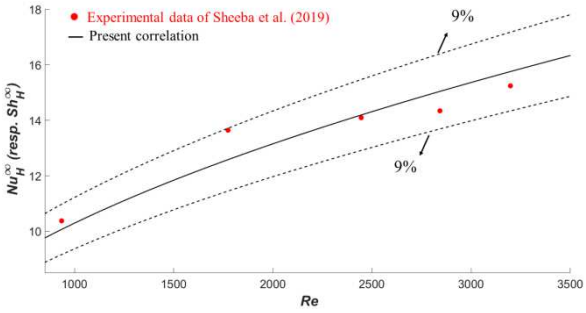

Figure 13: Comparison between the present correlation predictions and the experimental data of Sheeba and coworkers [23].

Differences between the correlation and the experimental results are due to several reasons, mainly the assumption of uniform fluid properties in CFD simulations, the accuracy of the current correlation and experimental errors. However, as can be noticed from Figure 8, the data of Ghobadi and Muzychka [22] are systematically overestimated by the current model. This is probably due to the experimental procedure they followed. Indeed, Ghobadi and Muzychka [22] placed their helical coil within a non-agitated water bath which temperature was maintained at 40 °C. For calculating the convective heat transfer coefficient and the Nusselt number, they assumed the wall temperature of their helical pipe to be equal to 40°C. However, in the absence of an efficient agitation, the wall temperature can significantly deviate from that of the water bath, especially because the heat transfer coefficient in the internal flow is large. This leads to an underestimation of the experimentally measured Nu_H^∞ and probably explains the systematic deviation between their measurements and the actual correlation predictions.

4.5. Optimal packing density of helixes: results and correlation

As noted in Section 3, the dimensionless distance between closely packed helixes, a_{min}^*, was determined using a CAD software for different helixes geometries. Figure 14 shows the contour plot of the interpolated results. The lowest possible value for a_{min}^* is 1, and is achieved with straight tubes, i.e. when R_H^* is zero or when p^* tends to infinity. a_{min}^* obviously increases when R_H^* is increased as can be noticed from Figure 6 for example. When p^* is increased, the spacing between the helixes turns enlarges. Hence, the helixes can be brought closer and imbricate, which leads to a decrease of a_{min}^* (as can be noticed from Figure 15).

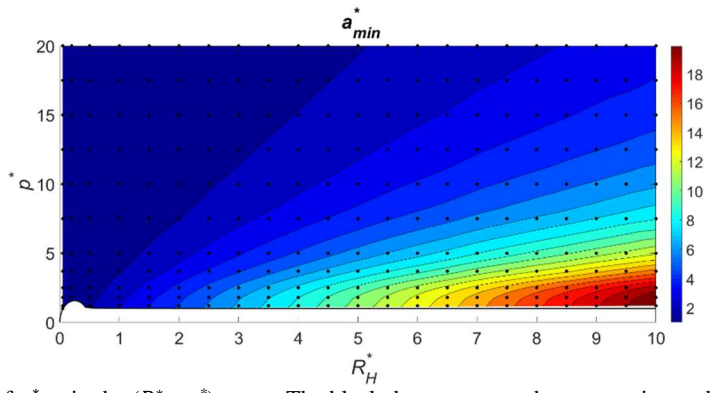

Figure 14: Contour plot of a^*_{min} in the (R^*_H , p^*) space. The black dots represent the geometric conditions for which CAD results are acquired.

To the authors' knowledge, the only available correlation for determining a^*_{min} or the helixes packing density is that reported in Kaufhold et al. [26]. However, the effects of the helix pitch are not taken into account in this correlation. Thus, it obviously lacks accuracy since a^*_{min} can be very sensitive to p^* value as can be noticed from Figure 14. Therefore, a regression model for a^*_{min} is proposed in this paper. The following mathematical expression, constructed by trial-and-error, was found to provide the best fit of the CAD data:

where:

$$a^*_{min} = 1 + A\, tanh\left(B\ \ p^{*C}\right)$$
$$A = p_1\, R^*_H + p_2$$
$$B = p_3\, R^{*\,p_4}_H$$
$$C = p_5\, \ln(\, R^*_H\,) + p_6 \qquad \text{Eq. 16}$$

The present expression includes 6 regression parameters denoted p_i (i being an integer ranging from 1 to 6) which values were determined using an optimization procedure in order to minimize the maximum relative difference between the correlation outputs and the CAD data. The hyperbolic tangent term is formulated so as to vanish when R^*_H tends to zero or when p^* tends to infinity. Accordingly, the correlation correctly predicts that a^*_{min} equals one at these limits.

The mathematical expression presented in Equations 16 was used to correlate the CAD data which were obtained in the following range of dimensionless parameters: $1 \le p^* \le 20$ and $0.05 \le R^*_H \le 10$. The optimization problem was solved using a genetic algorithm and the results were further refined using a local optimizer, GRG2. For a better accuracy, two correlations were derived, depending on whether R^*_H is lower or higher than 2 respectively. The optimal sets of the parameters p_i are reported in Table 4. An Excel sheet where the present correlation is implemented is provided as supplementary material to this paper.

Table 4: Optimal sets of the parameters of the correlation expressed by Equations 16.

Validity range	p_1	p_2	p_3	p_4	p_5	p_6
$0 \le R^*_H \le 2$	1.88	-5.54×10^{-2}	3.50	5.65×10^{-1}	-1.65×10^{-2}	-1.50
$2 \le R^*_H \le 10$	2.04	-3.65×10^{-1}	4.44	0	1.35×10^{-1}	-1.52

An excellent agreement between the model and the CAD results is obtained (Figure 15) as their maximal relative difference is 2.80% for R^*_H below 2 and 4.30% for R^*_H above 2 respectively. To check the robustness of the correlation, additional a^*_{min} computations (provided as supplementary material) were performed for p^* up to 1 000 and R^*_H up to 500. The model was able to predict all of these data with within a maximum error margin of 4.5% which demonstrates its predictive capacity.

(a) (b)

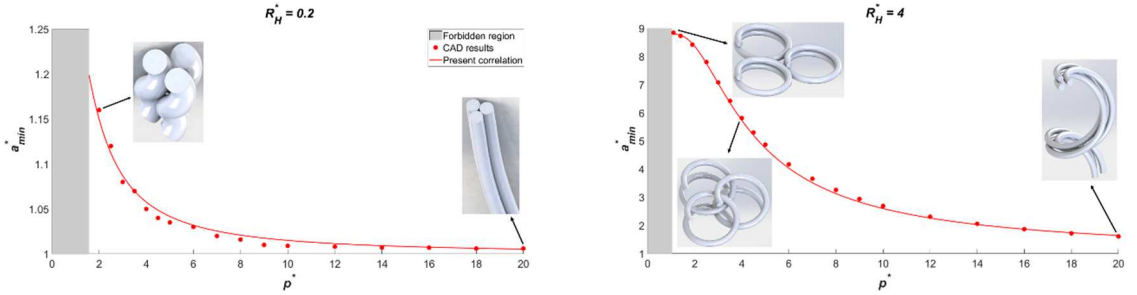

Figure 15: a^*_{min} versus p^* at (a) R^*_H = 0.2 and (b) R^*_H = 4: comparison between the CAD results and the present correlation (Equations 16).

The contour plot of a^*_{min} was calculated using the present model (Equations 16) and is given in Figure 16a. The current correlation along with Equation 12 were used to determine the helixes optimal packing density, $\phi_{H,max}$, in the (R^*_H , p^*) space. The contour plot of the $\phi_{H,max}$ to $\phi_{S,max}$ ratio is given in Figure 16b. $\phi_{S,max}$ is the optimal packing density of straight tubes which approximately equals 90.7%.

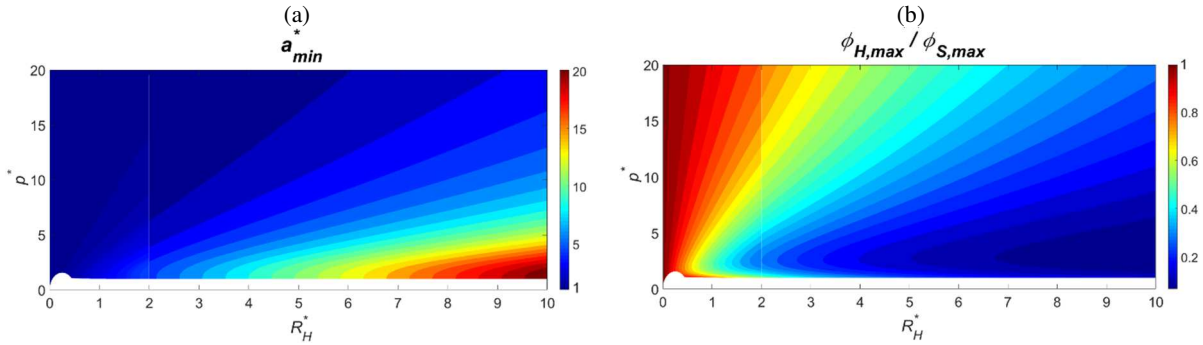

Figure 16: Contour plots in the (R^*_H , p^*) space of (a) a^*_{min} and (b) of the $\phi_{H,max}$ to $\phi_{S,max}$ ratio as calculated using the present model (Equations 16).

Figure 16b shows that the $\phi_{H,max}$ to $\phi_{S,max}$ ratio is always lower than unity as helixes cannot be as efficiently packed as straight tubes. However, it can be noticed that highly curved helixes allow considerably higher packing densities than classical ones, and thus, they provide much larger specific surface areas for heat/mass transfer. As HCHPs also lead to higher transfer efficiencies, they are by far more advantageous than classical ones in term of process intensification.

Figure 16b also reveals that apart for very low R^*_H, when p^* is increased, $\phi_{H,max}$ first decreases to a minimum before starting to increase. This is explained by the fact that increasing the helix pitch engenders additional void between the helix turns on the one hand, and on the other hand, the larger space between the helix turns allows the different helixes to be brought closer together. However, at very low pitches, this additional spacing enables the helixes to slightly approach only but not to imbricate. Therefore, the overall volume fraction filled by the helixes decreases. Once a sufficient p^* is reached, further increasing the helix pitch allow the helixes to better imbricate (Figure 15) which increases their optimal packing density.

4.6. Overall intensification factor and potentiality of highly curved helical pipes designs

As shown in the previous sections, HCHPs lead to great transfer efficiencies but cannot be as densely packed as straight tubes. These two aspects should be combined together for quantifying the volumetric transfer rate enhancement that these designs allow achieving when used in packed modules, i.e. for assessing the enabled unit volume reduction of reactors, heat exchangers or membrane contactors. Accordingly, the following intensification factor, ε, is proposed:

$$\varepsilon = \frac{Nu_H^{\infty}\,\phi_{H,max}}{Nu_S^{\infty}\,\phi_{S,max}} \quad or \quad \varepsilon = \frac{Sh_H^{\infty}\,\phi_{H,max}}{Sh_S^{\infty}\,\phi_{S,max}} \qquad \text{Eq. 17}$$

For a same tube diameter, it can be analytically shown that the $\phi_{H,max}$ to $\phi_{S,max}$ ratio equals the ratio of the specific surface area of helical and straight pipes. For a same fluid, the Nu_H^{∞} to Nu_S^{∞} (resp. Sh_H^{∞} to Sh_S^{∞}) ratio is

equal to the ratio of the heat (resp. mass) transfer coefficients in helical and straight tubes respectively. Thus, ε physically represents the ratio of the heat/mass flux achieved in helical pipes to that achieved in straight ones. For example, an $\varepsilon = 2$ indicates that the use of HCHPs allows obtaining similar transfer performance than straight tubes while reducing the volume of the heat/mass transfer device by nearly a factor 2. This is true whenever the heat/mass transfer resistance in the internal fluid side is the one that limits the overall transfer rate. This situation is commonly encountered in heat exchangers. It also occurs in many mass transfer devices, e.g. fluid degassing in membrane contactors under vacuum operation and fluid dispensing systems based on vaporization (e.g. pure liquid on the shell side of a contactor).

Figure 17 shows the contour plot of ε in the (R_H^*, p^*) plane for different fluid properties and operating conditions. Note that different scales are used for each subfigure. Figures 17a and 17b reveal that, at very low *Re*, HCHPs allow a moderate improvement of the transfer rates only, while classical helixes perform even worse than straight tubes. The reason is that, at low *Re*, centrifugal effects are moderate and thus generate Dean vortices of low intensity. Therefore, the provided heat/mass transfer enhancement remains limited and barely compensates the effects of the decrease of the packing density.

The intensification factor improves with increasing *Re* and *Pr* (resp. *Sc*) numbers. For *Re* = 2 000 for example, HCHPs achieve volumetric transfer rates nearly 6.5 times higher than straight tubes for *Pr* (resp. *Sc*) = 1 (Figure 17c), and the intensification factor exceeds 8 for *Pr* (resp. *Sc*) = 10 (Figure 17d). These results demonstrate the huge potential of HCHPs for process intensification.

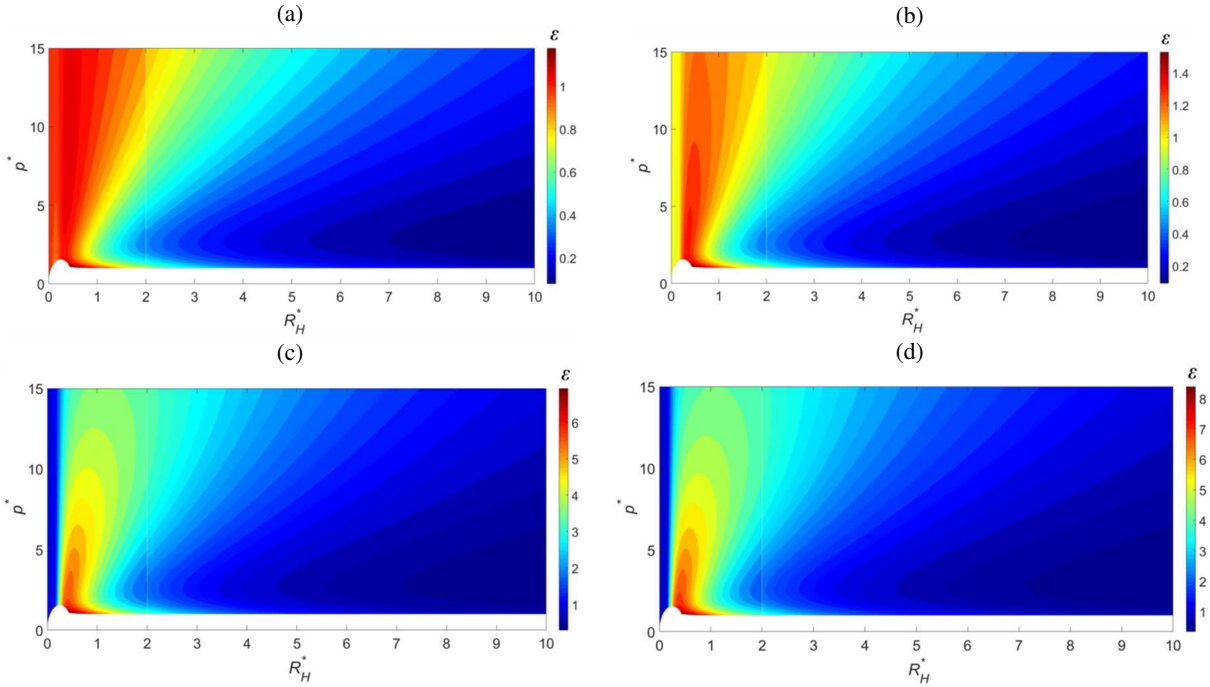

Figure 17: Contour plots of the intensification factor, ε, for: (a) *Re* = 10 and *Pr* (resp. *Sc*) = 1. (b) *Re* = 10 and *Pr* (resp. *Sc*) = 10. (c) *Re* = 2 000 and *Pr* (resp. *Sc*) = 1. (d) *Re* = 2 000 and *Pr* (resp. *Sc*) = 10.

5. Conclusion and perspectives

This paper focused on the heat/mass transfer enhancement in helical pipes, especially highly curved ones, under laminar flow conditions. Novel designs, offering huge potentialities for intensified mass and/or heat transfer performance have been identified: on the one hand, they generate intense Dean-type vortices, and on the other hand, they can be densely packed. The results demonstrate that highly curved helixes allow intensifying the volumetric transfer rate up to a factor 8, which should enable a massive unit volume reduction of reactors, heat exchangers and membrane contactors, as soon as the mass or heat transfer resistance is mostly located in the internal fluid (bore side). This situation is likely to occur in gas-liquid heat exchangers, catalytic reactors with large reaction rates, fluid degassing in membrane contactors under vacuum operation, or fluid dispensing systems based on vaporization (e.g. pure liquid on the shell side of a contactor).

Future studies by the authors will concentrate on the following points:

1- Experimental measurements of the heat/mass transfer efficiency in HCHPs (highly curved helical pipes) for a trustworthy validation of the present numerical results. Indeed, as explained in this paper, such data lack in the literature since HCHPs are difficult to manufacture using traditional manufacturing techniques. However,

nowadays, thanks to a witnessed progress in 3D-printing, the fabrication of such designs has become achievable [14].

2- The current paper showed that the heat/mass transfer efficiency in HCHPs considerably improves when the Prandtl/Schmidt number is increased. Therefore, it is worthwhile investigating the performance of these designs for fluids with higher Prandtl (e.g. oils) or Schmidt (e.g. liquids) numbers since enormous intensification factors may be expected [32].

3- Although intense Dean vortices in HCHPs lead to improved heat and mass transfer efficiencies compared to straight tubes, they also induce higher pressure drops and hence involve greater pumping costs. Therefore a multi-objective optimization is necessary to compare the benefits provided by HCHPs with the additional operating costs involved, and thus, assessing the potential of these designs. The correlations provided in this paper and in Abushammala et al. [14] allow determining the Nusselt/Schmidt number and the friction factor in helical pipes, and can thus be used as surrogates in this intended model-based optimization.

Acknowledgment

The authors gratefully thank the 'French ministry of higher education and research' for funding this study.

Nomenclature

a_{min}	Distance separating two closely packed helixes (m)
C_A	Molar concentration of A (mol m^{-3})
d	Pipe diameter (m)
D	Mass diffusivity (m^2 s^{-1})
De_{R_H}	Dean number following the definition of Eq. 14 (-)
De_γ	Dean number following the definition of Eq. 15 (-)
h	Heat transfer coefficient (W m^{-2} K^{-1})
k	Mass transfer coefficient (m s^{-1})
L_{th}	Length of the thermal entrance region (m)
$\dot{m}$	Mass flow rate (kg s^{-1})
$\vec{n}_A$	Mass flux of component A (kg m^{-2} s^{-1})
Nu	Nusselt number (-)
Nu_H^∞	Asymptotic Nusselt number in helical pipes (-)
Nu_S^∞	Asymptotic Nusselt number in straight pipes (-)
p	Helix pitch (m)
P	Pressure (Pa)
Pr	Prandtl number (-)
R_H	Helix radius (m)
Re	Reynolds number (-)
Sc	Schmidt number (-)
Sh	Sherwood number (-)
Sh_H^∞	Asymptotic Sherwood number in helical pipes (-)
Sh_S^∞	Asymptotic Sherwood number in straight pipes (-)
T	Temperature (K)
$T_{f,MC}$	Mixing-cup temperature (K)
T_w	Temperature of the wall (K)
$\vec{u}$	Fluid velocity vector (m s^{-1})
U	Mean velocity of the primary flow (m s^{-1})
$\vec{v}$	Bulk motion velocity (m s^{-1})
V	Volume (m^3)

Greek letters

α	Thermal diffusivity (m^2 s^{-1})
γ	Radius of curvature of the pipe (m)
ρ	Density (kg m^{-3})
ε	Intensification factor (-)
κ	Pipe curvature (m^{-1})
λ	Thermal conductivity (W m^{-1} K^{-1})
μ	Dynamic viscosity (Pa s)
ν	Kinematic viscosity (m^2 s^{-1})
ρ_A	Mass concentration of A (kg m^{-3})
$\phi_{H,max}$	Optimal packing density of helical pipes (-)
$\phi_{S,max}$	Optimal packing density of straight pipes (-)

Φ	Heat flux (W)

Superscripts

*	Designates a dimensionless number

References

[1] Alam T., Kim M. H., 2018. A comprehensive review on single phase heat transfer enhancement techniques in heat exchanger applications. *Renewable and Sustainable Energy Reviews*, 81, 813-839.

[2] Ghidossi R., Veyret D., Moulin, P., 2006. Computational fluid dynamics applied to membranes: State of the art and opportunities. *Chemical Engineering and Processing: Process Intensification*, 45(6), 437-454.

[3] Qiu L., Deng H., Sun J., Tao Z., Tian S., 2013. Pressure drop and heat transfer in rotating smooth square U-duct under high rotation numbers. *International journal of heat and mass transfer*, 66, 543-552.

[4] Khosravi-Bizhaem H., Abbassi A., Ravan A. Z., 2019. Heat transfer enhancement and pressure drop by pulsating flow through helically coiled tube: An experimental study. *Applied Thermal Engineering*, 160, 114012.

[5] Jaisankar S., Radhakrishnan T. K., Sheeba K. N., 2009. Experimental studies on heat transfer and friction factor characteristics of thermosyphon solar water heater system fitted with spacer at the trailing edge of twisted tapes. *Applied Thermal Engineering*, 29(5-6), 1224-1231.

[6] Yakut K., Sahin B., Celik C., Alemdaroglu N., Kurnuc, A., 2005. Effects of tapes with double-sided delta-winglets on heat and vortex characteristics. *Applied energy*, 80(1), 77-95.

[7] Ilyas M., Aydogan F., 2017. Steam generator performance improvements for integral small modular reactors. *Nuclear Engineering and Technology*, 49(8), 1669-1679.

[8] Kong R., Deethayat T., Asanakham A., Kiatsiriroat T., 2018. Heat transfer phenomena on waste heat recovery of combustion stack gas with deionized water in helical coiled heat exchanger. *Case studies in thermal engineering*, 12, 213-222.

[9] Javadi H., Ajarostaghi S. S. M., Pourfallah M., Zaboli M., 2019. Performance analysis of helical ground heat exchangers with different configurations. *Applied Thermal Engineering*, 154, 24-36.

[10] Abdel-Aziz M. H., Mansour I. A. S., Sedahmed, G. H., 2010. Study of the rate of liquid–solid mass transfer controlled processes in helical tubes under turbulent flow conditions. *Chemical Engineering and Processing: Process Intensification*, 49(7), 643-648.

[11] Mendez D. L. M., Lemaitre C., Castel C., Ferrari M., Simonaire H., Favre E., 2017. Membrane contactors for process intensification of gas absorption into physical solvents: Impact of dean vortices. *Journal of Membrane Science*, 530, 20-32.

[12] Mansour M., Liu Z., Janiga G., Nigam K. D., Sundmacher K., Thévenin D., Zähringer, K., 2017. Numerical study of liquid-liquid mixing in helical pipes. *Chemical Engineering Science*, 172, 250-261.

[13] Przybył S., Pierański P., 2001. Helical close packings of ideal ropes. *The European Physical Journal E*, 4(4), 445-449.

[14] Abushammala O., Hreiz R., Lemaitre C., Favre É., 2019. Laminar flow friction factor in highly curved helical pipes: Numerical investigation, predictive correlation and experimental validation using a 3D-printed model. *Chemical Engineering Science*, *207*, 1030-1039.

[15] Schmidt E. F., 1967. Wärmeübergang und druckverlust in rohrschlangen. *Chemie Ingenieur Technik*, 39(13), 781-789. [in German]

[16] Dravid A. N., Smith K. A., Merrill E. W., Brian P. L. T., 1971. Effect of secondary fluid motion on laminar flow heat transfer in helically coiled tubes. *AIChE Journal*, 17(5), 1114-1122.

[17] Kalb C. E., Seader J. D., 1974. Fully developed viscous—flow heat transfer in curved circular tubes with uniform wall temperature. *AIChE Journal*, 20(2), 340-346.

[18] Manlapaz R. L., Churchill, S. W., 1981. Fully developed laminar convection from a helical coil. *Chemical Engineering Communications*, 9(1-6), 185-200.

[19] Moulin P., Rouch J. C., Serra C., Clifton M. J., Aptel P., 1996. Mass transfer improvement by secondary flows: Dean vortices in coiled tubular membranes. *Journal of Membrane Science*, 114(2), 235-244.

[20] Yildiz, C., Biçer, Y., & Pehlivan, D., 1997. Heat transfer and pressure drop in a heat exchanger with a helical pipe containing inside springs. *Energy conversion and management*, 38(6), 619-624.

[21] Xin R. C., Ebadian M. A., 1997. The effects of Prandtl numbers on local and average convective heat transfer characteristics in helical pipes. *Journal of heat transfer*, 119(3), 467-473.

[22] Ghobadi M., Muzychka, Y. S., 2014. Fully developed heat transfer in mini scale coiled tubing for constant wall temperature. *International Journal of Heat and Mass Transfer*, 72, 87-97.

[23] Sheeba A., Abhijith C.M., Prakash M.J., 2019. Experimental and numerical investigations on the heat transfer and flow characteristics of a helical coil heat exchanger. *International Journal of Refrigeration*, 99, pp.490-497.

[24] Ghobadi M., Muzychka Y. S., 2016. A review of heat transfer and pressure drop correlations for laminar flow in curved circular ducts. *Heat Transfer Engineering*, 37(10), 815-839.

[25] Sabelfeld M., Geißen S. U., 2019. Effect of helical structure on ozone mass transfer in a hollow fiber membrane contactor. *Journal of membrane science*, *574*, 222-234.

[26] Kaufhold D., Kopf F., Wolff C., Beutel S., Hilterhaus L., Hoffmann M., Beutel S., Hilterhaus L., Hoffmann M., Scheper T., Schlüter M., Liese, A., 2012. Generation of Dean vortices and enhancement of oxygen transfer rates in membrane contactors for different hollow fiber geometries. *Journal of membrane science*, 423, 342-347.

[27] Kreith F., Boehm R. F., Raithby G. D., Hollands, K. G.T., Suryanarayana N. V., Modest M. F., Carey V. P., Chen J. C., Lior N., Shah R. K., Bell K.J., Moffat R. J., Mills A. F., Bergles A. E., Swanson L. W., Antonetti V. W., Irvine T. F., Capobianchi M., 1999. Heat and Mass Transfer Handbook. CRC Press, Boca Raton, Florida, USA.

[28] Saffari H., Moosavi R., Nouri N. M., Lin C. X., 2014. Prediction of hydrodynamic entrance length for single and two-phase flow in helical coils. *Chemical Engineering and Processing: Process Intensification*, 86, 9-21.

[29] Nusselt W., 1910. The dependence of the heat-transfer coefficient on tube length. Zeit. VDI, 54, 1154-1158. [in German]

[30] Jamshidi N., Farhadi M., Ganji D. D., Sedighi, K., 2013. Experimental analysis of heat transfer enhancement in shell and helical tube heat exchangers. *Applied thermal engineering*, 51(1-2), 644-652.

[31] De Amicis J., Cammi A., Colombo L. P., Colombo M., Ricotti M. E., 2014. Experimental and numerical study of the laminar flow in helically coiled pipes. *Progress in Nuclear Energy*, 76, 206-215.

[32] Abushammala O., Hreiz R., Lemaitre C., Favre É., 2019. Maximizing Mass Transfer Using Highly Curved Helical Pipes: A CFD Investigation. *6th International Conference of Fluid Flow, Heat and Mass Transfer,* Ottawa, Canada, June 2019.

Correlation for Nu / Sh number in helical pipes

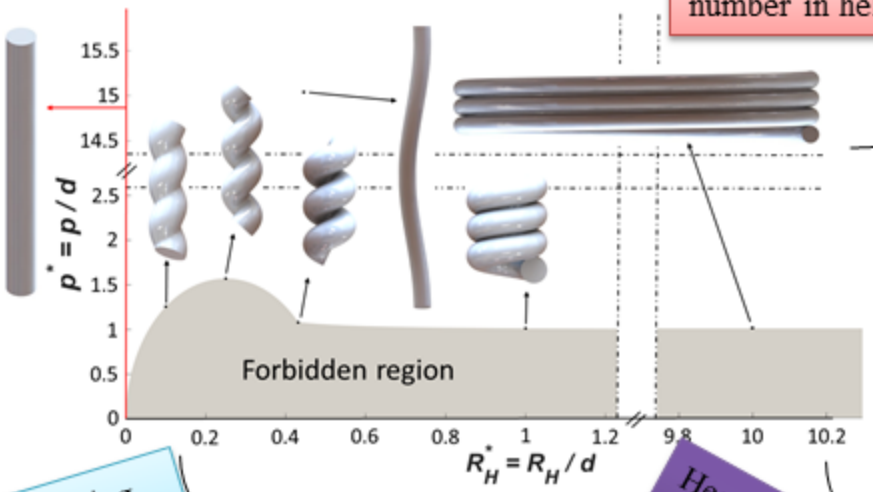

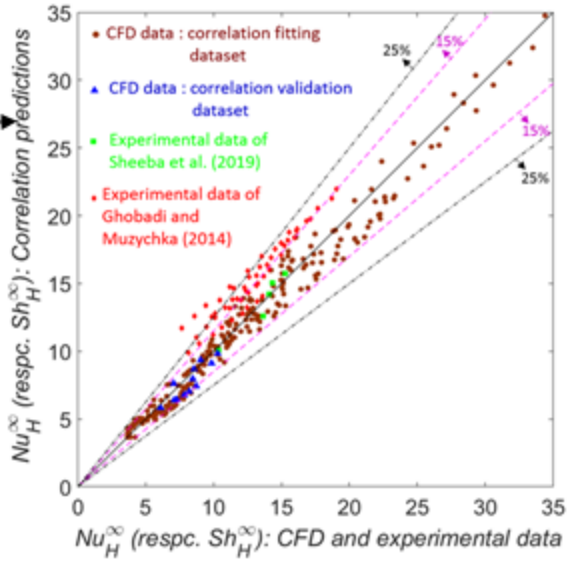

Packing density of helixes

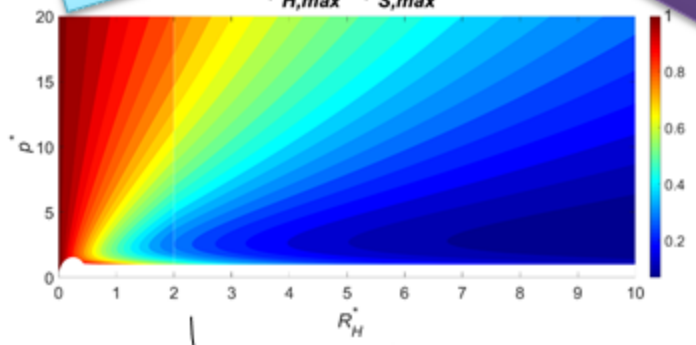

Heat/mass transfer in helical pipes

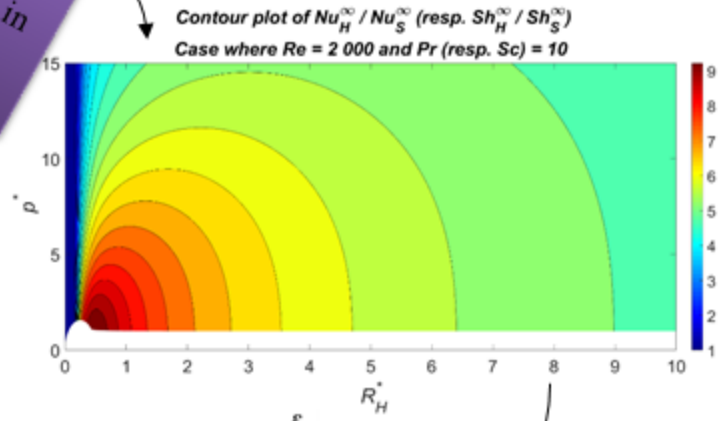

Overall intensification factor

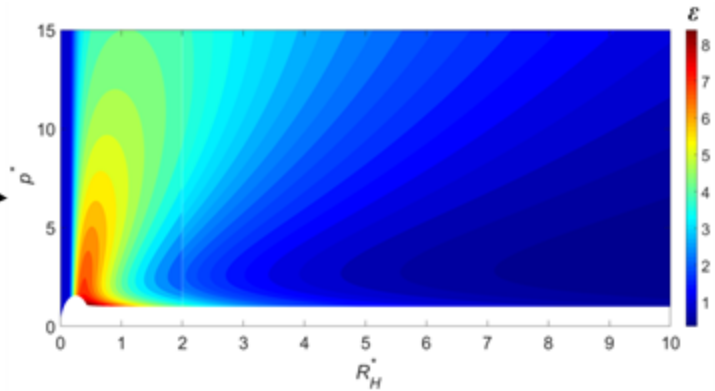

$$\varepsilon = \frac{Nu_H^\infty \, \phi_{H,max}}{Nu_S^\infty \, \phi_{S,max}} \quad \text{or} \quad \varepsilon = \frac{Sh_H^\infty \, \phi_{H,max}}{Sh_S^\infty \, \phi_{S,max}}$$